

Phonon-induced localization of excitons in molecular crystals from first principles

Antonios M. Alvertis,^{1,2,*} Jonah B. Haber,² Edgar A. Engel,³ Sahar Sharifzadeh,^{4,5} and Jeffrey B. Neaton^{1,2,6,†}

¹*Materials Sciences Division, Lawrence Berkeley National Laboratory, Berkeley, California 94720, USA*

²*Department of Physics, University of California Berkeley, Berkeley, United States*

³*Cavendish Laboratory, University of Cambridge,*

J. J. Thomson Avenue, Cambridge CB3 0HE, United Kingdom

⁴*Division of Materials Science and Engineering, Boston University, United States*

⁵*Department of Electrical and Computer Engineering, Boston University, United States*

⁶*Kavli Energy NanoScience Institute at Berkeley, Berkeley, United States*

(Dated: January 31, 2023)

The spatial extent of excitons in molecular systems underpins their photophysics and utility for optoelectronic applications. Phonons are reported to lead to both exciton localization and delocalization. However, a microscopic understanding of phonon-induced (de)localization is lacking, in particular how localized states form, the role of specific vibrations, and the relative importance of quantum and thermal nuclear fluctuations. Here we present a first-principles study of these phenomena in solid pentacene, a prototypical molecular crystal, capturing the formation of bound excitons, exciton-phonon coupling to all orders, and phonon anharmonicity, using density functional theory, the *ab initio* GW-Bethe-Salpeter equation approach, finite difference, and path integral techniques. We find that for pentacene zero-point nuclear motion causes uniformly strong localization, with thermal motion providing additional localization only for Wannier-Mott-like excitons. Anharmonic effects drive temperature-dependent localization, and while such effects prevent the emergence of highly delocalized excitons, we explore the conditions under which these might be realized.

Introduction.— Photoexcitation of organic molecular crystals leads to strongly bound electron-hole pairs, or excitons, due to the weak screening of the Coulomb interaction in these systems. Depending on factors such as the size of the molecular building blocks and the spin of the electron-hole pair, exciton radii can vary from those of localized Frenkel excitons [1, 2] to spatially extended excitons that approach the Wannier-Mott limit [3–7]. The spatial extent of these excited states is important to applications of organic semiconductors such as photovoltaics [8] and LEDs [9], since it affects properties including the nature of their interaction with phonons [10], their transport [11] and non-radiative recombination [12].

Critical to affecting the spatial extent of excited states are lattice vibrations, which are generally thought to result in wavefunction localization [13]. Phonons can strongly renormalize one- and two-particle excitation energies of organic systems, influencing the optical gap and the charge carrier mobility [10, 14, 15]. Phonons in these systems have generally been thought to lead to localized excitons that diffuse via, *e.g.*, a Förster or Dexter mechanism [16, 17]. However, it has recently been proposed that in certain well-ordered organic crystals atomic motion can give rise to configurations that favor strong transient exciton delocalization, having a beneficial effect to transport [18–20]. This transient exciton delocalization is similar to transient *charge* delocalization [21–23], wherein phonons lead to configurations with large overlaps between neighboring molecular orbitals [24] and

hence highly delocalized states [25].

Despite these insights, a rigorous microscopic understanding of phonon-induced modulations to exciton radii, one that accounts for electron-hole interactions, strong exciton-phonon coupling at finite temperatures [10, 26], and the anharmonicity of low-frequency motions in molecular crystals [27–30], is still lacking. Here we elucidate the microscopic mechanism of exciton localization in extended molecular solids. We employ a first-principles computational framework which captures all aforementioned effects, combining density functional theory (DFT), the Green’s function-based *ab initio* GW-Bethe Salpeter equation (BSE) approach for accurately describing exciton effects [31], finite-difference methods for strong exciton-phonon interactions [10, 32], and path integral techniques for describing phonon anharmonicity [33, 34]. We apply this framework to the prototypical molecular crystal pentacene and show that zero-point nuclear motion leads to strong localization of singlet and triplet excitons, reducing their average electron-hole separation by more than a factor of two. Temperature increases further reduce the size of delocalized Wannier-Mott-like excitons, an effect driven by anharmonic phonons. The trends in exciton radii are reflected in the dispersion of their energies in reciprocal space. While highly delocalized excitons do appear at large phonon displacements, anharmonicity reduces the amplitude associated with these motions, suppressing transient delocalization for exciton transport.

System and methods.— We focus on the widely studied molecular crystal pentacene [35], which hosts a delocalized Wannier-Mott-like singlet exciton (Fig. 1a) and a more localized Frenkel-like triplet exciton (Fig. 1b) [7,

* amalvertis@lbl.gov

† jbneaton@lbl.gov

[10, 36], for which the effect of phonons is expected to be different. We compute excitons with principal quantum number S and center-of-mass momentum \mathbf{Q} using *ab initio* DFT and *GW*-BSE calculations with the Quantum Espresso [37] and BerkeleyGW [38] codes. This involves constructing the electron-hole kernel K^{e-h} and solving the BSE [31, 39] in reciprocal space in the electron-hole basis, namely

$$\begin{aligned} & (E_{c\mathbf{k}+\mathbf{Q}} - E_{v\mathbf{k}}) A_{cv\mathbf{k}\mathbf{Q}}^S \quad (1) \\ & + \sum_{c'v'\mathbf{k}'} \langle c\mathbf{k} + \mathbf{Q}, v\mathbf{k} | K^{e-h} | c'\mathbf{k}' + \mathbf{Q}, v'\mathbf{k}' \rangle A_{c'v'\mathbf{k}'\mathbf{Q}}^S \\ & = \Omega_{\mathbf{Q}}^S A_{cv\mathbf{k}\mathbf{Q}}^S, \end{aligned}$$

with input from prior DFT and *GW* calculations. In Eq. 1 the indices c, v define conduction and valence states respectively, \mathbf{k} is the crystal momentum, and $A_{cv\mathbf{k}\mathbf{Q}}^S$ is the amplitude contributed by states c, v with momentum \mathbf{k} to the exciton with momentum \mathbf{Q} . The exciton wavefunction can be written as

$$\Psi_{\mathbf{Q}}^S(\mathbf{r}_e, \mathbf{r}_h) = \sum_{cv\mathbf{k}} A_{cv\mathbf{k}\mathbf{Q}}^S \psi_{c\mathbf{k}+\mathbf{Q}}(\mathbf{r}_e) \psi_{v\mathbf{k}}^*(\mathbf{r}_h), \quad (2)$$

where $\psi_{n\mathbf{k}}$ are the Kohn-Sham wavefunctions. The kernel K^{e-h} consists only of an attractive ‘direct’ term between electrons and holes for triplets, while for singlets it also includes a repulsive ‘exchange’ term, giving singlets their greater spatial extent [7, 31]. The energies of the conduction and valence bands in Eq. 1 are obtained within the so-called *GW* approximation [40] from self-energy corrections to DFT Kohn-Sham eigenvalues. This approach has been shown to give highly accurate descriptions of excitons in molecular crystals [7, 10, 36, 41, 42]. The computational details for our DFT and *GW*-BSE calculations are given in Supplemental Material [43] Section S1.

We treat the effect of phonons following Monserrat [32, 44, 45], and in a manner similar in spirit to Zacharias and Giustino [46, 47]. For an observable \mathcal{O} at a temperature T , we compute the ensemble-average in the adiabatic approximation as

$$\langle \mathcal{O}(T) \rangle_{\mathcal{H}} = \frac{1}{Z} \int dX \mathcal{O}(X) e^{-\beta \mathcal{H}}, \quad (3)$$

where the canonical partition function $Z = \int dX e^{-\beta \mathcal{H}}$ involves the configuration space integral $\int dX$ [48]. Non-adiabatic effects to the electron-phonon interactions of organic systems such as pentacene are negligible [49].

The Hamiltonian \mathcal{H} of the system includes electronic and nuclear degrees of freedom in general, and may be approximated at different levels. One approach is to assume nuclear motion to be harmonic, reducing the phonon con-

tribution to the Hamiltonian to the following form,

$$\mathcal{H}^{\text{har}} \equiv \frac{1}{2} \sum_{n,\mathbf{q}} (\nabla_{u_{n,\mathbf{q}}}^2 + \omega_{n,\mathbf{q}}^2 u_{n,\mathbf{q}}^2), \quad (4)$$

in atomic units. Here, phonons of frequencies ω are labeled by their branch index n and wavevector \mathbf{q} . We compute the ensemble-average $\langle \mathcal{O}^{\text{har}} \rangle$ in the Born-Oppenheimer approximation, tracing out all electronic degrees of freedom, using a finite-displacements approach [50, 51] to calculate phonon frequencies $\{\omega_{n,\mathbf{q}}\}$ and eigendisplacements $\{u_{n,\mathbf{q}}\}$, and then drawing N random samples $\{X_i^{\text{har}}\}$ from the multivariate Gaussian phonon distribution and calculating the observables of interest $\{\mathcal{O}(X_i^{\text{har}})\}$. $\langle \mathcal{O}^{\text{har}} \rangle$ is then simply computed as the average of its value at the samples

$$\langle \mathcal{O}^{\text{har}} \rangle = \lim_{N \rightarrow \infty} \frac{1}{N} \sum_{i=1}^N \mathcal{O}(X_i^{\text{har}}). \quad (5)$$

Eqs. 4 and 5 are exact apart from the adiabatic and harmonic approximations, and the description of phonon effects on any observable \mathcal{O} in Eq. 5 is non-perturbative [26].

The use of the harmonic approximation in molecular crystals can lead to unphysical results, due to highly anharmonic behavior of low-frequency phonons [27, 29]. In this work, we account for this anharmonicity by employing path-integral molecular dynamics (PIMD) which are rendered computationally tractable using the surrogate machine-learning (ML) potential V^{ML} from Refs. [27, 52], constructed to reproduce the potential energy surface (PES) from first-principles density functional theory (DFT) calculations. The modified phonon Hamiltonian

$$\mathcal{H}^{\text{anhar}} \equiv \sum_{i=1}^{N_a} \frac{\hat{\mathbf{p}}_i^2}{2m_i} + V^{\text{ML}}(\hat{\mathbf{r}}_1, \dots, \hat{\mathbf{r}}_{N_a}) \quad (6)$$

is used to run PIMD simulations at reduced computational cost, for a cell of N_a atoms, with nucleus i having a mass m_i , and $\hat{\mathbf{p}}_i, \hat{\mathbf{r}}_i$ its momentum and position operators respectively. We then draw random samples from the PIMD trajectories, and use these to compute vibrational averages of observables, analogously to Eq. 5, namely

$$\langle \mathcal{O}^{\text{anhar}} \rangle = \lim_{N \rightarrow \infty} \frac{1}{N} \sum_{i=1}^N \mathcal{O}(X_i^{\text{anhar}}). \quad (7)$$

Our simulations use a $2 \times 1 \times 1$ supercell of pentacene ($N_a = 144$ atoms), capturing the effect of phonons at Γ and at the band-edge X on observables. Phonons beyond Γ and X have a minor effect on pentacene optical properties as discussed in Supplemental Material [43] Section S1.C.

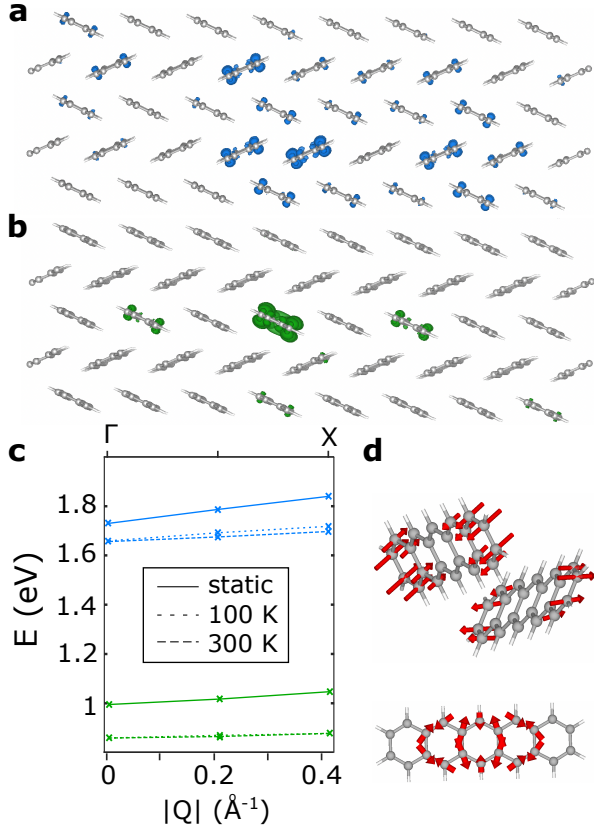


FIG. 1. Isosurfaces of electron distributions of singlet (blue, panel **a**) and triplet (green, panel **b**) excitons for a hole fixed at the center of the plotted area, and corresponding dispersions (panel **c**, same color scheme) in molecular crystals. A typical low-frequency (top) and high-frequency (bottom) phonon of pentacene is shown in panel **d**.

To quantify exciton localization, we study two observables \mathcal{O} . The first are the exciton energies at finite center-of-mass momentum, $\Omega_{\mathbf{Q}}^S$, obtained through solving the BSE (Eq. 1). The second is the average electron-hole separation for each excitation S , which we refer to as the exciton radius r_{exc} . This is obtained by post-processing the BSE solution Ψ_S , as discussed elsewhere [53] and in Supplemental Material [43] Section S1. To determine the exciton radius, we compute the electron-hole correlation function as defined in Ref. [53], namely

$$F_S(\mathbf{r}) = \int_V d\mathbf{r}_h |\Psi_S^{Q=0}(\mathbf{r}_e = \mathbf{r}_h + \mathbf{r}, \mathbf{r}_h)|^2, \quad (8)$$

where V the volume of the primitive cell. $F_S(\mathbf{r})$ describes the probability of finding the electron-hole pair at a distance of $\mathbf{r} = \mathbf{r}_e - \mathbf{r}_h$, and is computed as a discrete sum over hole positions. The average exciton radius for a given atomic configuration is then

$$r_{\text{exc}} = \int d|\mathbf{r}| F_S(|\mathbf{r}|) |\mathbf{r}|. \quad (9)$$

Having described the main quantities in our computational framework, we may summarize it as follows. We generate displaced configurations X_i^{har} within the harmonic approximation using a finite differences approach, and X_i^{anhar} within the anharmonic distribution through PIMD employing a previously-developed ML potential. The *ab initio* BSE, Eq. 1, is solved at these configurations, followed by a calculation of the exciton radius via Eq. 9. We then compute the vibrational averages using Eqs. 5 and 7. Details of the convergence of the vibrational averages, the ML potential, and PIMD simulations, are given in Supplemental Material [43] Section S1.

Results.— We first discuss exciton properties obtained from solving the BSE without consideration of phonons. We refer to these clamped-ion solutions as the ‘static’ case. Fig. 1 shows an isosurface of the electron density for the first singlet (S_1 , blue, panel **a**) and triplet (T_1 , green, panel **b**) exciton, for a hole fixed at the center of the visualized region. As shown previously [7, 10, 36], the singlet is significantly more delocalized than the triplet, which results in bands that are more dispersive in reciprocal space [7, 42], as shown in Fig. 1c. We plot the exciton energies along the path $\Gamma \rightarrow X$ in the Brillouin zone, corresponding to the dominant packing direction of the pentacene crystal. Table I summarizes the bandwidth $W = \Omega(X) - \Omega(\Gamma)$ of the two excitons, as well as the width $\Delta = \Omega(\mathbf{Q} = 0.4 \text{ \AA}^{-1}) - \Omega(\mathbf{Q} = 0.1 \text{ \AA}^{-1})$, the values of the exciton momentum chosen to accommodate comparison to recent experiments [54]. We see from our static calculations that the singlet bandwidth is more than twice that of the triplet.

We now include the effect of phonons on the exciton band structures along $\Gamma \rightarrow X$ at 100 K and 300 K, within the harmonic and anharmonic distributions, and visualize the results in Fig. 1c when including anharmonic effects. There are two broad categories of phonons in molecular crystals, corresponding to low-frequency intermolecular and high-frequency intramolecular motions, visualized in Fig. 1d. While the former are predominantly activated when going from 100 K to 300 K, the latter have significant zero-point energies $\hbar\omega/2$. Including 100 K phonon effects red-shifts both singlet and triplet exciton energies and flattens their dispersions, as shown in Fig. 1c and Table I. This effect is larger for the triplet, which is more localized and therefore more impacted by high-frequency intra-molecular modes. However, increasing the temperature to 300 K has no effect on the triplet, since there are negligible additional contributions from intramolecular modes at these temperatures and the modulations of intermolecular distances by lower-frequency phonons hardly affect this localized state. In contrast, the delocalized singlet red-shifts further, and its dispersion flattens by an additional 18 meV. Our results for the singlet width Δ at 100 K are in excellent agreement with recent experiments [54], as summarized in Table I. Our predicted decrease of the singlet width Δ by 13 meV when increasing the temperature from 100 K to 300 K underestimates the experimental decrease of

| | $W^{\text{anhar}}(S_1)$ (meV) | $W^{\text{har}}(S_1)$ (meV) | $W^{\text{anhar}}(T_1)$ (meV) | $\Delta^{\text{anhar}}(S_1)$ (meV) | $\Delta^{\text{exp}}(S_1)$ (meV) [54] |
|--------|-------------------------------|-----------------------------|-------------------------------|------------------------------------|---------------------------------------|
| static | 110 | 110 | 52 | 80 | — — — |
| 100 K | 59 | 67 | 18 | 43 | 44 |
| 300 K | 41 | 76 | 19 | 30 | 23 |

TABLE I. The effect of phonons on the dispersion width $W = \Omega(X) - \Omega(\Gamma)$ for the first singlet Ω_S and triplet Ω_T excitons of pentacene, and on the width $\Delta = \Omega(\mathbf{Q} = 0.4 \text{ \AA}^{-1}) - \Omega(\mathbf{Q} = 0.1 \text{ \AA}^{-1})$ for the singlet.

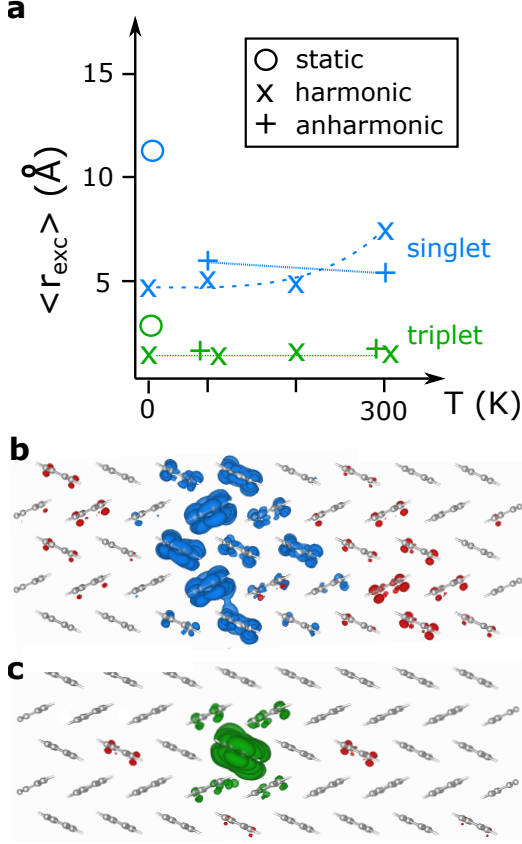


FIG. 2. Singlet (blue) and triplet (green) exciton radii within the different cases and temperatures (panel a). Representative configuration showing electronic isosurfaces for fixed hole positions, indicating localization of the singlet (triplet) at 0 K towards the region in blue (green), shown in panel b (panel c). Red represents electronic wavefunction amplitude that disappears in the presence of phonons.

21 meV, largely due to ignoring thermal expansion in our calculation, which reduces Δ by a further 6 meV within this temperature range, see Supplemental Material [43] Section S2. Interestingly, we see in Table I that the harmonic approximation predicts an *increase* of the singlet bandwidth with increasing temperature, contrary to our calculations including anharmonic effects using PIMD and to experiment, a point that we return to below.

The changes in the width of the exciton dispersions suggest phonon-induced modulations of real-space exciton properties, which are zero-point dominated for the triplet, and which have significant temperature depen-

dence for the singlet. We highlight the connection between the dispersion modulations and real-space exciton properties by computing vibrational averages of the exciton radii at a range of temperatures. The results are presented in Fig. 2 for the singlet (blue) and triplet (green) within the harmonic approximation and including anharmonic effects. Let us first comment on the harmonic case. Compared to the static limit (circles), the radii in the presence of phonons at 0 K are renormalized by more than a factor of two. For the singlet, the static value of 11.2 Å for its radius reduces to 4.9 Å, while the static triplet radius of 2.7 Å reduces to 1.2 Å. To visualize this we present in Fig. 2b and Fig. 2c differential plots for iso-surfaces of the electron density once a hole is placed at a high-probability position in the unit cell. Specifically, we plot the difference between the electronic density of the case without phonons and that of a typical atomic configuration at 0 K. Red indicates amplitude vanishing due to phonons, while blue and green indicate areas where the singlet and triplet wavefunction respectively gain amplitude, demonstrating their tendency to localize.

When increasing the temperature to 300 K within the harmonic approximation there is no change to the triplet exciton radius, in agreement with our expectation of the effect of phonons on the triplet exciton dispersion. The singlet however exhibits delocalization, with its radius increasing substantially to the average value of 6.96 Å, consistent with the increase of the singlet bandwidth with temperature in the harmonic case. Upon including anharmonic effects, triplet radii agree with the harmonic case; however, for the singlet the results are qualitatively different, and we recover the expected behavior of decreasing singlet radius with increasing temperature. All vibrational averages and errors for the exciton radii are given in Section S7 of the Supplemental Material [43].

The discrepancy between the harmonic and anharmonic cases is due to configurations with highly delocalized excitons within the harmonic approximation, with radii as large as 31 Å at 300 K. Such configurations are shown in Supplementary Material [43] Section S5, and their inclusion in the thermal averages of Eq. 5 for the radii leads to the observed temperature-induced increase of $\langle r_{\text{exc}} \rangle$ in Fig. 2a. To understand why such configurations are not present within the anharmonic case, we plot in Fig. 3a the difference between the phonon root mean squared displacement $\sqrt{\langle u^2 \rangle}$ of the two distributions at 300 K. We find that a low-frequency acoustic mode, corresponding to a sliding along the z-axis of adjacent pentacene molecules, is significantly over-displaced

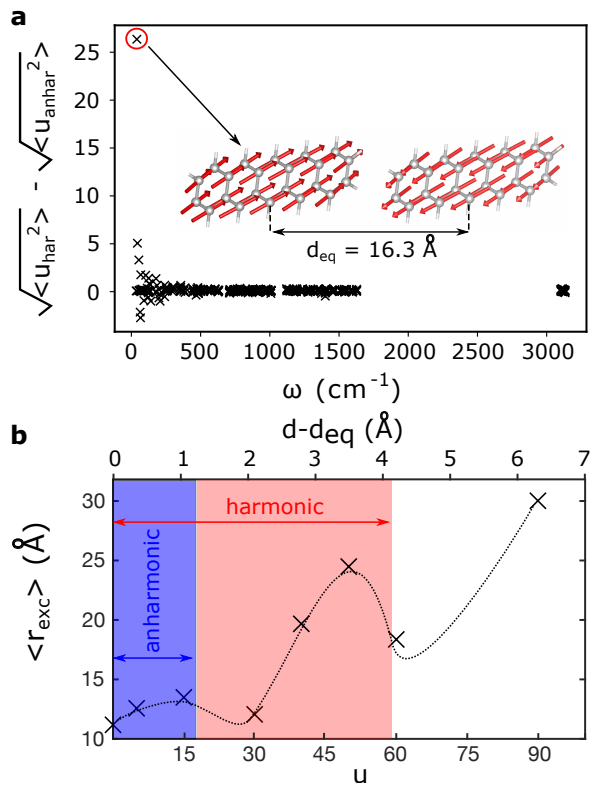


FIG. 3. The difference between the RMS displacement of phonons in the harmonic and anharmonic distributions of pentacene (panel a). Singlet exciton radii (panel b) along the highly anharmonic phonon shown in panel a. Phonon displacements u are given in units of their zero-point width $1/\sqrt{2\omega_{qv}}$ [32]. The dotted line in b is a guide to the eye.

in the harmonic case at $\mathbf{q} = X$. Anharmonic terms alter the PES associated with this phonon, limiting its average amplitude at room temperature, as shown in Supplementary Material [43] Fig. S3, in agreement with known cases where the harmonic approximation breaks down in molecular crystals [27, 29, 30]. We confirm that the over-displacement of this phonon within the harmonic approximation leads to the temperature-induced singlet delocalization observed in Fig. 2a, by computing the singlet radius as a function of amplitude of this mode, as visualized in Fig. 3b. The blue and red regions indicate the maximum range of displacements which are accessible within the anharmonic and harmonic distributions respectively, due to thermal excitation of phonons at 300 K. The harmonic approximation leads to configurations with highly

delocalized excitons of radii as large as 25 Å. The dependence of the exciton radius on the phonon displacement is non-monotonic due to the oscillating π orbital overlap between neighboring pentacene molecules [55].

While highly delocalized excitons may appear at certain nuclear configurations, anharmonicity prevents accessing these, as seen in Fig. 3b. However, such configurations could appear out of equilibrium, *e.g.* due to photoexcitation, upon relaxation to the excited state PES minimum. For pentacene, the minimum of the singlet exciton PES along the anharmonic acoustic mode lies far from the ‘delocalized’ region of Fig. 3b (see Supplemental Material [43] Section S6), it is thus unlikely that for this and similar systems transiently delocalized excitons may be accessed, even outside equilibrium.

Conclusions.— We have presented a first-principles study of the effect of phonons on the dispersion and radii of excitons in the prototypical molecular crystal pentacene. Zero-point nuclear motion uniformly causes substantial localization of excitons, manifesting as a flattening of the exciton dispersion in reciprocal space. Wannier-Mott-like singlet excitons also exhibit additional temperature-activated localization due to their stronger coupling to low-frequency phonons, with anharmonic effects being critical in capturing this effect and preventing transient exciton delocalization. Anharmonic low-frequency phonons are common in molecular materials [27] and can couple to singlets when these approach the Wannier-Mott limit, in a manner which is in turn determined by the size [10] and packing [56] of the molecular building blocks. Our work lays foundations for a deep understanding and controlled enhancement of exciton transport in molecular crystals, for example by suppressing anharmonicity through chemical modifications [57].

We thank Sivan Refaely-Abramson for useful discussions. This work was primarily supported by the Theory FWP, which provided *GW* and *GW*-BSE calculations and analysis of phonon effects, and the Center for Computational Study of Excited-State Phenomena in Energy Materials (C2SEPPEM), which provided advanced codes, at the Lawrence Berkeley National Laboratory, funded by the U.S. Department of Energy, Office of Science, Basic Energy Sciences, Materials Sciences and Engineering Division, under Contract No. DE-AC02-05CH11231. SS acknowledges funding from the U.S. National Science Foundation (NSF) under grant number DMR-1847774. Computational resources were provided by the National Energy Research Scientific Computing Center (NERSC).

- [1] J. Frenkel, On the transformation of light into heat in solids. i, *Phys. Rev.* **37**, 17 (1931).
- [2] J. Frenkel, On the transformation of light into heat in solids. ii, *Phys. Rev.* **37**, 1276 (1931).
- [3] G. H. Wannier, The structure of electronic excitation levels in insulating crystals, *Phys. Rev.* **52**, 191 (1937).

- [4] N. F. Mott, Conduction in polar crystals. II. The conduction band and ultra-violet absorption of alkali-halide crystals, *Trans. Faraday Soc.* **34**, 500 (1938).
- [5] P. Cudazzo, M. Gatti, and A. Rubio, Excitons in molecular crystals from first-principles many-body perturbation theory: Picene versus pentacene, *Phys. Rev. B* **86**,

- 1 (2012).
- [6] P. Cudazzo, M. Gatti, A. Rubio, and F. Sottile, Frenkel versus charge-transfer exciton dispersion in molecular crystals, *Phys. Rev. B* **88**, 1 (2013).
- [7] P. Cudazzo, F. Sottile, A. Rubio, and M. Gatti, Exciton dispersion in molecular solids, *Journal of Physics Condensed Matter* **27**, 10.1088/0953-8984/27/11/113204 (2015).
- [8] A. Distler, C. J. Brabec, and H. J. Egelhaaf, Organic photovoltaic modules with new world record efficiencies, *Progress in Photovoltaics: Research and Applications* **29**, 24 (2021).
- [9] S. Reineke, F. Lindner, G. Schwartz, N. Seidler, K. Walzer, B. Lüssem, and K. Leo, White organic light-emitting diodes with fluorescent tube efficiency., *Nature* **459**, 234 (2009).
- [10] A. M. Alvertis, R. Pandya, L. A. Muscarella, N. Sawhney, M. Nguyen, B. Ehrler, A. Rao, R. H. Friend, A. W. Chin, and B. Monserrat, Impact of exciton delocalization on exciton-vibration interactions in organic semiconductors, *Phys. Rev. B* **102**, 081122 (2020).
- [11] J. Aragón and A. Troisi, Dynamics of the excitonic coupling in organic crystals, *Physical Review Letters* **114**, 1 (2015).
- [12] G. Kupgan, X. K. Chen, and J. L. Brédas, Molecular Packing in the Active Layers of Organic Solar Cells Based on Non-Fullerene Acceptors: Impact of Isomerization on Charge Transport, Exciton Dissociation, and Nonradiative Recombination, *ACS Applied Energy Materials* **4**, 4002 (2021).
- [13] P. W. Anderson, Absence of diffusion in certain random lattices, *Phys. Rev.* **109**, 1492 (1958).
- [14] F. Brown-Altvater, G. Antonius, T. Rangel, M. Giantomassi, C. Draxl, X. Gonze, S. G. Louie, and J. B. Neaton, Band gap renormalization, carrier mobilities, and the electron-phonon self-energy in crystalline naphthalene, *Phys. Rev. B* **101**, 1 (2020).
- [15] G. Schweicher, G. D’Avino, M. T. Ruggiero, D. J. Harkin, K. Broch, D. Venkateshvaran, G. Liu, A. Richard, C. Ruzié, J. Armstrong, A. R. Kennedy, K. Shankland, K. Takimiya, Y. H. Geerts, J. A. Zeitler, S. Fratini, and H. Sirringhaus, Chasing the “Killer” Phonon Mode for the Rational Design of Low-Disorder, High-Mobility Molecular Semiconductors, *Advanced Materials* **31**, 10.1002/adma.201902407 (2019).
- [16] S. Athanasopoulos, E. V. Emelianova, A. B. Walker, and D. Beljonne, Exciton diffusion in energetically disordered organic materials, *Phys. Rev. B* **80**, 1 (2009).
- [17] L. Sudha Devi, M. K. Al-Suti, C. Dosche, M. S. Khan, R. H. Friend, and A. Köhler, Triplet energy transfer in conjugated polymers. I. Experimental investigation of a weakly disordered compound, *Phys. Rev. B* **78**, 1 (2008).
- [18] A. J. Sneyd, T. Fukui, D. Paleček, S. Prodhan, I. Wagner, Y. Zhang, J. Sung, S. M. Collins, T. J. Slater, Z. Andaji-Garmaroudi, L. R. MacFarlane, J. D. Garcia-Hernandez, L. Wang, G. R. Whittell, J. M. Hodgkiss, K. Chen, D. Beljonne, I. Manners, R. H. Friend, and A. Rao, Efficient energy transport in an organic semiconductor mediated by transient exciton delocalization, *Science Advances* **7**, 10.1126/sciadv.abh4232 (2021).
- [19] S. Giannini, W.-T. Peng, L. Cupellini, D. Padula, A. Carof, and J. Blumberger, Exciton transport in molecular organic semiconductors boosted by transient quantum delocalization, *Nature Communications* **13**, 1 (2022).
- [20] A. J. Sneyd, D. Beljonne, and A. Rao, A New Frontier in Exciton Transport : Transient Delocalization, *Journal of Physical Chemistry Letters* **13**, 6820 (2022).
- [21] S. Fratini, D. Mayou, and S. Ciuchi, The transient localization scenario for charge transport in crystalline organic materials, *Advanced Functional Materials* **26**, 2292 (2016), 1505.02686.
- [22] Y. Zhang, C. Liu, A. Balaeff, S. S. Skourtis, and D. N. Beratan, Biological charge transfer via flickering resonance, *Proceedings of the National Academy of Sciences of the United States of America* **111**, 10049 (2014).
- [23] D. N. Beratan, Why Are DNA and Protein Electron Transfer So Different?, *Annual Review of Physical Chemistry* **70**, 71 (2019).
- [24] A. Troisi, G. Orlandi, and J. E. Anthony, Electronic interactions and thermal disorder in molecular crystals containing cofacial pentacene units, *Chemistry of Materials* **17**, 5024 (2005).
- [25] S. Giannini, A. Carof, M. Ellis, H. Yang, O. G. Ziegler, S. Ghosh, and J. Blumberger, Quantum localization and delocalization of charge carriers in organic semiconducting crystals, *Nature Communications* **10**, 1 (2019).
- [26] B. Monserrat, E. A. Engel, and R. J. Needs, Giant electron-phonon interactions in molecular crystals and the importance of nonquadratic coupling, *Phys. Rev. B* **92**, 1 (2015).
- [27] A. M. Alvertis and E. A. Engel, Importance of vibrational anharmonicity for electron-phonon coupling in molecular crystals, *Phys. Rev. B* **105**, 1 (2022).
- [28] H. Seiler, M. Krynski, D. Zahn, S. Hammer, Y. W. Windsor, T. Vasileiadis, J. Pflaum, R. Ernstorfer, M. Rossi, and H. Schwoerer, Nuclear dynamics of singlet exciton fission: a direct observation in pentacene single crystals, *Science Advances* **7**, eabg0869 (2021).
- [29] J. H. Fetherolf, P. Shih, and T. C. Berkelbach, Conductivity of an electron coupled to anharmonic phonons, *arXiv* (2022).
- [30] M. Rossi, P. Gasparotto, and M. Ceriotti, Anharmonic and Quantum Fluctuations in Molecular Crystals: A First-Principles Study of the Stability of Paracetamol, *Phys. Rev. Lett.* **117**, 115702 (2016).
- [31] M. Rohlfing and S. G. Louie, Electron-hole excitations and optical spectra from first principles, *Phys. Rev. B* **62**, 4927 (2000), 0406203v3 [arXiv:cond-mat].
- [32] B. Monserrat, Electron – phonon coupling from finite differences, *Journal of Physics Condensed Matter* **30** (2018).
- [33] V. Kapil, J. Behler, and M. Ceriotti, High order path integrals made easy, *The Journal of Chemical Physics* **145**, 234103 (2016).
- [34] M. Ceriotti, M. Parrinello, T. E. Markland, and D. E. Manolopoulos, Efficient stochastic thermostating of path integral molecular dynamics, *J. Chem. Phys.* **133**, 124104 (2010).
- [35] S. Haas, B. Batlogg, C. Besnard, M. Schiltz, C. Kloc, and T. Siegrist, Large uniaxial negative thermal expansion in pentacene due to steric hindrance, *Phys. Rev. B* **76**, 1 (2007).
- [36] S. Refaely-Abramson, F. H. Da Jornada, S. G. Louie, and J. B. Neaton, Origins of Singlet Fission in Solid Pentacene from an ab initio Green’s Function Approach, *Physical Review Letters* **119**, 1 (2017), 1706.01564.
- [37] P. Giannozzi, S. Baroni, N. Bonini, M. Calandra, R. Car, C. Cavazzoni, D. Ceresoli, G. L. Chiarotti, M. Cococ-

- cioni, I. Dabo, A. Dal Corso, S. Fabris, G. Fratesi, S. de Gironcoli, R. Gebauer, U. Gerstmann, C. Gougoussis, A. Kokalj, M. Lazzeri, L. Martin-Samos, N. Marzari, F. Mauri, R. Mazzarello, S. Paolini, A. Pasquarello, L. Paulatto, C. Sbraccia, S. Scandolo, G. Sclauzero, A. P. Seitsonen, A. Smogunov, P. Umari, and R. M. Wentzcovitch, *QUANTUM ESPRESSO: a modular and open-source software project for quantum simulations of materials*, *Journal of Physics: Condensed Matter* **21**, 395502 (2009).
- [38] J. Deslippe, G. Samsonidze, D. A. Strubbe, M. Jain, M. L. Cohen, and S. G. Louie, BerkeleyGW: A massively parallel computer package for the calculation of the quasiparticle and optical properties of materials and nanostructures, *Computer Physics Communications* **183**, 1269 (2012), 1111.4429.
- [39] D. Y. Qiu, G. Cohen, D. Novichkova, and S. Refaely-Abramson, Signatures of Dimensionality and Symmetry in Exciton Band Structure: Consequences for Exciton Dynamics and Transport, *Nano Letters* **21**, 7644 (2021).
- [40] M. S. Hybertsen and S. G. Louie, Electron correlation in semiconductors and insulators: Band gaps and quasiparticle energies, *Phys. Rev. B* **34**, 5390 (1986).
- [41] T. Rangel, K. Berland, S. Sharifzadeh, F. Brown-Altvater, K. Lee, P. Hyldgaard, L. Kronik, and J. B. Neaton, Structural and excited-state properties of oligoacene crystals from first principles, *Phys. Rev. B* **93**, 1 (2016).
- [42] T. Lettmann and M. Rohlfing, Finite-momentum excitons in rubrene single crystals, *Phys. Rev. B* **104**, 1 (2021).
- [43] See supplemental material at [url will be inserted by the production group] which includes references [10, 27, 34, 36–38, 41, 44, 52, 53, 58–68] for computational details.
- [44] B. Monserrat, Vibrational averages along thermal lines, *Phys. Rev. B* **93**, 1 (2016), 1512.06377.
- [45] B. Monserrat, Correlation effects on electron-phonon coupling in semiconductors: Many-body theory along thermal lines, *Phys. Rev. B* **93**, 10.1103/PhysRevB.93.100301 (2016), 0703642 [astro-ph].
- [46] M. Zacharias and F. Giustino, One-shot calculation of temperature-dependent optical spectra and phonon-induced band-gap renormalization, *Phys. Rev. B* **94**, 10.1103/PhysRevB.94.075125 (2016), 1604.02394.
- [47] M. Zacharias and F. Giustino, Theory of the special displacement method for electronic structure calculations at finite temperature, *Physical Review Research* **2**, 7 (2020), 1912.10929.
- [48] C. E. Patrick and F. Giustino, Unified theory of electron-phonon renormalization and phonon-assisted optical absorption, *Journal of Physics: Condensed Matter* **26**, 365503 (2014).
- [49] A. Miglio, V. Brousseau-Couture, E. Godbout, G. Antonius, Y. H. Chan, S. G. Louie, M. Côté, M. Giantomassi, and X. Gonze, Predominance of non-adiabatic effects in zero-point renormalization of the electronic band gap, *npj Computational Materials* **6**, 10.1038/s41524-020-00434-z (2020), 2011.12765.
- [50] G. Kresse, J. Furthmüller, and J. Hafner, Ab initio Force Constant Approach to Phonon Dispersion Relations of Diamond and Graphite, *Europhysics Letters* **32**, 729 (1995).
- [51] K. Parlinski, Z. Q. Li, and Y. Kawazoe, First-Principles Determination of the Soft Mode in Cubic ZrO_2 , *Physical Review Letters* **78**, 4063 (1997).
- [52] V. Kapil and E. A. Engel, A complete description of thermodynamic stabilities of molecular crystals, *Proc. Natl. Acad. Sci. U.S.A.* **119**, e2111769119 (2022).
- [53] S. Sharifzadeh, P. Darancet, L. Kronik, and J. B. Neaton, Low-Energy Charge-Transfer Excitons in Organic Solids from First-Principles: The Case of Pentacene, *The Journal of Physical Chemistry Letters* **4**, 2197 (2013).
- [54] L. Graf, A. Kusber, B. Büchner, and M. Knupfer, Strong exciton bandwidth reduction in pentacene as a function of temperature, *Phys. Rev. B* **106**, 165429 (2022).
- [55] J. Aragón and A. Troisi, Regimes of exciton transport in molecular crystals in the presence of dynamic disorder, *Advanced Functional Materials* **26**, 2316 (2016).
- [56] S. Sharifzadeh, C. Y. Wong, H. Wu, B. L. Cotts, L. Kronik, N. S. Ginsberg, and J. B. Neaton, Relating the Physical Structure and Optoelectronic Function of Crystalline TIPS-Pentacene, *Advanced Functional Materials* **25**, 2038 (2015).
- [57] M. Asher, R. Jouclas, M. Bardini, Y. Diskin-posner, N. Kahn, R. Korobko, A. R. Kennedy, L. S. D. Moraes, G. Schweicher, J. Liu, D. Beljonne, Y. Geerts, and O. Ya, Chemical Modifications Suppress Anharmonic Effects in the Lattice Dynamics of Organic Semiconductors, *ACS Materials Au* **10.1021/acsmaterialsau.2c00020** (2022).
- [58] S. Haas, B. Batlogg, C. Besnard, M. Schiltz, C. Kloc, and T. Siegrist, Large uniaxial negative thermal expansion in pentacene due to steric hindrance, *Phys. Rev. B* **76**, 1 (2007).
- [59] J. P. Perdew, K. Burke, and M. Ernzerhof, Generalized Gradient Approximation Made Simple, *Physical Review Letters* **77**, 3865 (1996).
- [60] H. J. Monkhorst and J. D. Pack, Special points for Brillouin-zone integrations, *Phys. Rev. B* **13**, 5188 (1976).
- [61] A. Tkatchenko and M. Scheffler, Accurate molecular van der Waals interactions from ground-state electron density and free-atom reference data, *Physical Review Letters* **102**, 6 (2009).
- [62] Y. Eldar, M. Lindenbaum, M. Porat, and Y. Y. Zeevi, The Farthest Point Strategy for Progressive Image Sampling, *IEEE Transactions on Image Processing* **6**, 1305 (1997).
- [63] R. J. G. B. Campello, D. Moulavi, A. Zimek, and J. Sander, Hierarchical density estimates for data clustering, visualization, and outlier detection, *ACM Trans. Knowl. Discov. Data* **10**, 5 (2015).
- [64] A. P. Bartók, R. Kondor, and G. Csányi, On representing chemical environments, *Phys. Rev. B* **87**, 184115 (2013).
- [65] M. J. Willatt, F. Musil, and M. Ceriotti, Feature optimization for atomistic machine learning yields a data-driven construction of the periodic table of the elements, *Phys Chem Chem Phys* **20**, 29661 (2018).
- [66] A. Singraber, N2P2, <https://github.com/CompPhysVienna/n2p2>.
- [67] V. Kapil, M. Rossi, O. Marsalek, R. Petraglia, Y. Litman, T. Spura, B. Cheng, A. Cuzzocrea, R. H. Meißner, D. M. Wilkins, B. A. Helfrecht, P. Juda, S. P. Bienvenue, W. Fang, J. Kessler, I. Poltavsky, S. Vandenbrande, J. Wieme, and M. Ceriotti, i-PI 2.0: A universal force engine for advanced molecular simulations, *Computer Physics Communications* **236**, 214 (2018).
- [68] S. Plimpton, Fast parallel algorithms for short-range molecular dynamics, *J. Comput. Phys.* **117**, 1 (1995).

Supplemental Material: Phonon-induced localization of excitons in molecular crystals from first principles

Antonios M. Alvertis,^{1,2,*} Jonah B. Haber,² Edgar A. Engel,³ Sahar Sharifzadeh,^{4,5} and Jeffrey B. Neaton^{1,2,6,†}

¹*Materials Sciences Division, Lawrence Berkeley National Laboratory, Berkeley, California 94720, USA*

²*Department of Physics, University of California Berkeley, Berkeley, United States*

³*Cavendish Laboratory, University of Cambridge, J. J. Thomson Avenue, Cambridge CB3 0HE, United Kingdom*

⁴*Division of Materials Science and Engineering, Boston University, United States*

⁵*Department of Electrical and Computer Engineering, Boston University, United States*

⁶*Kavli Energy NanoScience Institute at Berkeley, Berkeley, United States*

CONTENTS

| | |
|---|----|
| S1. Computational details | 3 |
| A. DFT calculations | 3 |
| B. <i>GW</i> -BSE calculations | 3 |
| C. Phonon calculations and Monte Carlo sampling of vibrational averages | 3 |
| D. Machine learning potential and path-integral molecular dynamics | 6 |
| E. Calculation of exciton radii | 7 |
| S2. Effect of thermal expansion | 8 |
| S3. Contributions of Γ and X phonons | 9 |
| A. Exciton radii | 9 |
| B. Exciton dispersion | 10 |
| S4. Anharmonic potential energy surfaces | 11 |
| S5. Highly delocalized excitons within the harmonic approximation | 12 |
| S6. Estimation of the minimum of the singlet exciton potential energy surface | 12 |
| S7. Tables of averages and standard deviations of exciton energies and radii | 15 |
| References | 17 |

* amalvertis@lbl.gov

† jbneaton@lbl.gov

S1. COMPUTATIONAL DETAILS

A. DFT calculations

First-principles energies, forces, band gaps and wavefunctions are computed using the Quantum Espresso [1] DFT code with the semi-local PBE exchange-correlation functional [2] and a plane-wave energy cut-off of 60 Rydberg for the wavefunction. For the unit cell of pentacene we start from the experimental structure PENCEN08 as in the Cambridge Crystallographic Database [3], and relax the internal coordinates while leaving the volume fixed and using the Tkatchenko-Scheffler (TS) dispersion correction [4]. For the geometry optimization we employ a $4 \times 4 \times 2$ Monkhorst-Pack \mathbf{k} -point grid [5].

B. GW-BSE calculations

We employ the one-shot G_oW_o approximation for the quasiparticle properties of pentacene, as implemented in the BerkeleyGW code [6]. We use a $4 \times 4 \times 2$ k-grid, 400 bands and a 7 Ry plane wave cutoff to calculate the dielectric screening. For exciton calculations, we construct the electron-hole kernel on a $4 \times 4 \times 2$ grid using 4 valence and 4 conduction states, and then interpolate on a $8 \times 8 \times 4$ k-grid with the same number of bands. This set of parameters has been shown to give converged results in previous computational studies of pentacene [7, 8]. When studying $2 \times 1 \times 1$ supercells of pentacene (see following subsection on the Monte Carlo sampling of vibrational averages), we use a half the number of k-points in the x direction in all cases ($2 \times 4 \times 2$ to calculate the dielectric screening and $4 \times 8 \times 4$ to interpolate the BSE kernel), and double the number of bands for the dielectric screening (800 bands) and exciton calculations (8 valence and 8 conduction bands).

C. Phonon calculations and Monte Carlo sampling of vibrational averages

We include the contribution from lattice dynamics at temperature T to an observable \mathcal{O} by means of the quantum mechanical expectation value

$$\mathcal{O}(T) = \frac{1}{Z} \sum_{\mathbf{s}} \langle \chi_{\mathbf{s}}(\mathbf{u}) | \mathcal{O}(\mathbf{u}) | \chi_{\mathbf{s}}(\mathbf{u}) \rangle e^{-E_{\mathbf{s}}/k_{\text{B}}T}, \quad (1)$$

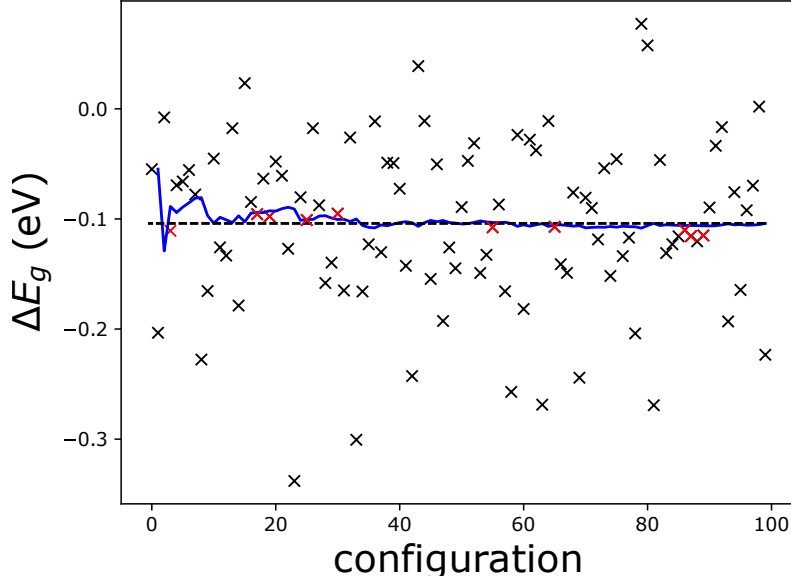


FIG. S1. Convergence of the DFT band gap renormalization ΔE_g as a function of the number of configurations used in the Monte Carlo sampling, for the example of using a $2 \times 1 \times 1$ supercell at $T = 100$ K. The value of the gap renormalization for each configuration is denoted in black crosses, while the blue line is the running average of the band gap renormalization due to phonons. The dashed line is the final computed average value for the band gap renormalization, while the red crosses indicate the ten configurations for which we run *GW*-BSE calculations to obtain their exciton properties.

where $|\chi_{\mathbf{s}}\rangle$ is the harmonic vibrational wavefunction in state \mathbf{s} with energy $E_{\mathbf{s}}$, $\mathcal{Z} = \sum_{\mathbf{s}} e^{-E_{\mathbf{s}}/k_{\text{B}}T}$ is the partition function, and $\mathbf{u} = \{u_{\mathbf{q}\nu}\}$ is a collective coordinate that includes the amplitudes of all normal modes of vibration in the system labeled by the phonon wave vector \mathbf{q} and the phonon branch ν .

Substituting the harmonic vibrational wavefunction, the above expectation value can be rewritten

$$\mathcal{O}(T) = \int d\mathbf{u} |\Phi(\mathbf{u}; T)|^2 \mathcal{O}(\mathbf{u}), \quad (2)$$

where:

$$|\Phi(\mathbf{u}; T)|^2 = \prod_{\mathbf{q}, \nu} (2\pi\sigma_{\mathbf{q}\nu}^2(T))^{-1/2} \exp\left(-\frac{u_{\mathbf{q}\nu}^2}{2\sigma_{\mathbf{q}\nu}^2(T)}\right), \quad (3)$$

the harmonic density at temperature T , which is a product of Gaussian functions of width:

$$\sigma_{\mathbf{q}\nu}^2(T) = \frac{1}{2\omega_{\mathbf{q}\nu}} \cdot \coth\left(\frac{\omega_{\mathbf{q}\nu}}{2k_B T}\right). \quad (4)$$

We evaluate Eq. (2) by generating stochastic samples distributed according to the harmonic vibrational ensemble, calculating the observable of interest at each configuration, and averaging over all configurations. To sample the single-particle DFT electronic band gap we generate 100 configurations, which are sufficient for convergence, as demonstrated in Fig. S1. We obtain the band gap correction for each of these configurations at temperatures of $T = 0$ K, $T = 100$ K, $T = 200$ K and $T = 300$ K. We then apply *GW* corrections to these DFT values. Due to the large computational cost of these calculations, we only perform *GW* calculations on the ten configurations whose single-particle DFT band gap value is closest to the calculated average band gap for each temperature, as also shown in Fig. S1. This correlated sampling strategy between DFT and *GW* has been shown to be accurate in pentacene [8] and other systems [9]. Having calculated the effects of electron-phonon coupling on the quasiparticle band gap, we solve the Bethe-Salpeter equation for the same ten configurations at the various temperatures, using the parameters of the previous section and computing exciton energies (at finite exciton momenta) and exciton radii.

The sampling of the expectation value of equation 2 becomes increasingly accurate with the inclusion of more \mathbf{q} -points in the Brillouin zone. Within the finite differences approach for phonon calculations and the expectation values of observables at finite temperatures, \mathbf{q} -points are described using commensurate supercells. For pentacene a $2 \times 1 \times 1$ (size 2) supercell (four pentacene molecules) is 98% converged with respect to a $2 \times 2 \times 2$ (size 8) supercell (sixteen molecules) for the band gap zero-point renormalization (-139 meV and -142 meV respectively), as seen in Fig. S2 where we plot the convergence of the pentacene band gap renormalization at 100 K, as obtained from sampling within the anharmonic distribution. Therefore a $2 \times 1 \times 1$ supercell offers a good balance between computational cost for the *GW*-BSE calculations, and accuracy.

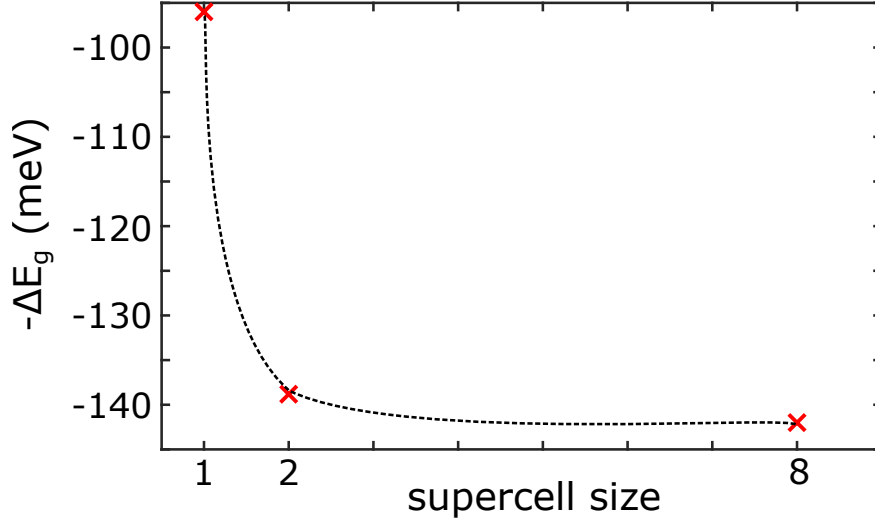


FIG. S2. Convergence of the pentacene DFT band gap renormalization ΔE_g at $T = 100$ K, as a function of the supercell size. The dashed line is given as a guide to the eye.

D. Machine learning potential and path-integral molecular dynamics

The details of the construction of the machine learning potential for pentacene (and other acene crystals), as well as the procedure for obtaining trajectories within path-integral molecular dynamics, have been described elsewhere [10]. Here we include some key points and refer the reader interested in a more in-depth discussion to Ref. [10].

A machine learning potential describing the dynamics of the acene series of molecular crystals was trained on a set of training data including the total energies of 4862 configurations of naphthalene, anthracene, tetracene and pentacene, obtained from the harmonic distributions at 0 K, 150 K, and 300 K. From this set, 400 validation and 400 test configurations were drawn randomly. For tuning the ML potential architecture and training procedure, the training data was sparsified by farthest-point-sampling (FPS) [11, 12], retaining the 1000 most structurally distinct training configurations. This FPS was performed on the basis of Euclidean distances between configurations described in terms of their smooth overlap of atomic positions (SOAP) powerspectra [13], using the radially-scaled implementation [14] with a radial and angular basis of 12 and nine functions, respectively, a cut-off radius of 8 Å, a width of 0.275 Å for the Gaussian densities associated with the atomic positions, and a scaling onset and exponent of 2.5 Å and 4.5, respectively. An ensemble of seven fully-connected, feed-forward neural networks with two hidden layers of 16 nodes each was constructed by using the N2P2 code [15].

For the independent testset, the ML potentials reproduce the reference energies and forces with root-mean-square errors of 2.4 meV/atom and 0.157 meV/Å, respectively. Crucially, this suffices to run stable path integral simulations in the constant-volume ensemble over extended simulation times, and to accurately compute the quantum-mechanical expectation values of observables within the reference first-principles thermodynamic ensemble.

Finite-temperature, quantum-mechanical thermodynamic averages of observables can be computed as averages of their values for (random) configurations drawn from PIMD simulations. We exploit the affordability of the ML potential to perform PIMD in the NVT ensemble at temperatures of 100 K and 300 K, and subsequently compute observables for configurations extracted from the PIMD trajectory (after equilibration) at regular intervals of 50 fs, which ensures that these samples are decorrelated. The PIMD simulations of at least 10 ps were performed using the i-PI [16] molecular dynamics engine to drive LAMMPS [17] energy and force evaluations of the ML potential, a 0.25 fs timestep, and a path integral Langevin equation thermostat [18] with $\tau = 100$ fs.

The number of replicas required for PIMD simulations is determined by the highest frequency phonon modes that are present in the system, which in our case is C–H stretching and is common among all acene crystals. For benzene it has been shown that 32 replicas are sufficient to converge electronic band gaps within 15 meV [10, 19], and the same value has therefore been employed for pentacene.

For obtaining the exciton properties (energies and radii) within the anharmonic distributions we follow a tactic similar to the correlated sampling described in the case of the harmonic Monte Carlo sampling. We first draw 100 configurations at which we compute the DFT band gap and then we rank the configurations based on their band gap proximity to the computed mean value. We then perform GW -BSE calculations on the top 10 configurations among these.

E. Calculation of exciton radii

As discussed in the main text, we compute the electron-hole correlation function as defined in Ref. [20], namely

$$F_S(\mathbf{r}) = \int_V d^3\mathbf{r}_h |\psi_S^{Q=0}(\mathbf{r}_e = \mathbf{r}_h + \mathbf{r}, \mathbf{r}_h)|^2, \quad (5)$$

where V the volume of the primitive cell. $F_S(\mathbf{r})$ describes the probability of finding the electron-hole pair at a vector $\mathbf{r} = \mathbf{r}_e - \mathbf{r}_h$, and is computed as a discrete sum over hole positions. We note here that even if we only integrate over the volume of the primitive cell, the exciton wavefunction can delocalize over the whole supercell used in the Bethe-Salpeter calculation, *i.e.*, $8 \times 8 \times 4$ or $4 \times 8 \times 4$ for pentacene, as discussed below. Even if the hole was moved outside the primitive cell, we would simply obtain a shifted exciton wavefunction.

For pentacene, it was found in Ref. [20] that the average electron-hole distance of the correlation function is converged, and that its envelope produces a smooth function for 88 high-probability hole positions in the unit cell, corresponding to two hole positions per carbon atom, at $\pm 0.5 \text{ \AA}$ above and below the plane of the molecule for each atom (effectively sampling the C p_z orbitals). For each sampled hole, the correlation function is computed on an $8 \times 8 \times 4$ supercell of pentacene, which is necessary for convergence of the exciton wavefunctions. For the $2 \times 1 \times 1$ cell of pentacene, which includes the effects of phonons (see section S1 C), the real-space supercell used for $F_S(\mathbf{r})$ is reduced to $4 \times 8 \times 4$, since every cell along the x direction already contains two unit cells. Moreover the number of carbon atoms per cell doubles, and so we sample at $88 \cdot 2 = 176$ hole positions in this case.

Having computed the electron-hole correlation function for a given atomic configuration \mathbf{u} , the exciton radius is computed as

$$r_{\text{exc}}(\mathbf{u}) = \int d\mathbf{r} |F_S(|\mathbf{r}|)|\mathbf{r}|. \quad (6)$$

To compute the vibrationally renormalized exciton radii at a temperature T , we apply equations 5 and 7 of the main manuscript with $\mathcal{O} = r_{\text{exc}}$. In the example case where we make the harmonic approximation this results in

$$\langle r_{\text{exc}}(T) \rangle = \int d\mathbf{u} |\Phi(\mathbf{u}; T)|^2 r_{\text{exc}}(\mathbf{u}), \quad (7)$$

where $|\Phi(\mathbf{u}; T)|^2$ the harmonic density function, as discussed in section S1 C above.

S2. EFFECT OF THERMAL EXPANSION

To study the effect of thermal expansion on the exciton dispersion of pentacene, we perform GW-BSE calculations on two pentacene structures deposited in the Cambridge

Crystallographic Database, which have been obtained through X-ray diffraction measurements at temperatures within the range of interest of 100 – 300 K. These are the structures PENCEN06 and PENCEN07 [3], obtained at 120 K and 293 K respectively. We use the experimental crystal structures without any optimization of the internal coordinates. The absolute value of the singlet exciton energy and width are known to be very sensitive to coordinate optimization and the precise level of theory employed to perform this optimization [21]. Therefore here we will focus on differences between energies and dispersion widths of the two experimental structures, without attempting a direct comparison to values obtained for the optimized structure necessary to perform phonon calculations. In principle phonons and thermal expansion need to be accounted for concurrently, however the large number of degrees of freedom in molecular crystals constitute such an analysis extremely challenging.

The dispersion width $W = E(X) - E(\Gamma)$ is found to be 11 meV smaller in the high-temperature phase. Given the linear character of the static exciton dispersion of pentacene, we can estimate the bandwidth $\Delta = \Omega(\mathbf{Q} = 0.4 \text{ \AA}^{-1}) - \Omega(\mathbf{Q} = 0.1 \text{ \AA}^{-1})$, and find that Δ for the singlet exciton shrinks by 6 meV due to thermal expansion within this range of temperatures. There is therefore no competition between thermal expansion and exciton-phonon coupling in terms of their effect on the exciton dispersion. Moreover, this flattening of the exciton dispersion caused by thermal expansion will bring the predicted value of $\Delta = 30 \text{ meV}$ for the width at 300 K and when including anharmonic effects, even closer to the experimental value of 23 meV at the same temperature (Table I, main manuscript).

S3. CONTRIBUTIONS OF Γ AND X PHONONS

A. Exciton radii

The values for the vibrationally renormalized exciton radii given in the main manuscript, in both the harmonic and anharmonic cases, include the effects of Γ and X phonons, *i.e.* include phonons within a $2 \times 1 \times 1$ supercell of pentacene. As shown in Fig. 2 of the main manuscript, the harmonic approximation predicts an increase of the average exciton radius with increasing the temperature from 0 K to 300 K. Qualitatively, this is in agreement with the case of only including the effect of Γ phonons within the harmonic approximation, *i.e.*

| $r_{\text{exc}}(T)$ (Å) | $1 \times 1 \times 1$ (Γ) | $2 \times 1 \times 1$ (Γ, X) |
|-------------------------|------------------------------------|---------------------------------------|
| 0 K | 4.73 ± 0.35 | 4.85 ± 0.30 |
| 300 K | 5.09 ± 0.40 | 6.96 ± 1.25 |

TABLE S1. The effect of Γ and X phonons on the vibrationally-averaged exciton radius, within the harmonic approximation.

| | $W(S_1)$ (meV) | $W(T_1)$ (meV) |
|--------|----------------|----------------|
| static | 110 | 52 |
| 100 K | 67 | 18 |
| 300 K | 59 | 19 |

TABLE S2. The effect of Γ phonons on the dispersion width W for the first singlet and triplet excitons of pentacene, including anharmonic effects.

focusing on a single unit cell of pentacene, as seen in Table S1. Quantitatively, this increase of the radius becomes more prevalent when including X phonons (in the $2 \times 1 \times 1$ supercell), which is to be expected given that anharmonic effects are more relevant for finite phonon wavevectors \mathbf{q} as discussed in the main manuscript and in Ref. [10].

B. Exciton dispersion

Tables S2 and S3 summarize the effect of Γ phonons only on the width $W = E(X) - E(\Gamma)$ of the exciton dispersion within the anharmonic and harmonic distributions respectively. The results given in Table I of the main manuscript also contain the effect of phonons at the band-edge X .

For both the harmonic and anharmonic cases, the result for the triplet is the same: the width of the exciton band narrows entirely due to zero-point motion, and increasing the temperature to 300 K has no effect on it. For the singlet, while we find that including anharmonic effects at 100 K leads to a greater band-narrowing compared to the harmonic case (at 0 K), increasing the temperature to 300 K leads to a further reduction of the bandwidth by 8 meV, compared to the 12 meV of the harmonic case. For the exact values of the exciton energies please refer to the tables of section S7. It is also worth noting that in this case of including Γ phonons only, the harmonic approximation does not show the unphysical increase of the dispersion width with increasing temperature, due to not including the highly anharmonic acoustic phonon at $\mathbf{q} = X$, see also section S4.

| | $W(S_1)$ (meV) | $W(T_1)$ (meV) |
|--------|----------------|----------------|
| static | 110 | 52 |
| 0 K | 82 | 20 |
| 300 K | 70 | 19 |

TABLE S3. The effect of Γ phonons on the dispersion width W for the first singlet and triplet excitons of pentacene, within the harmonic approximation.

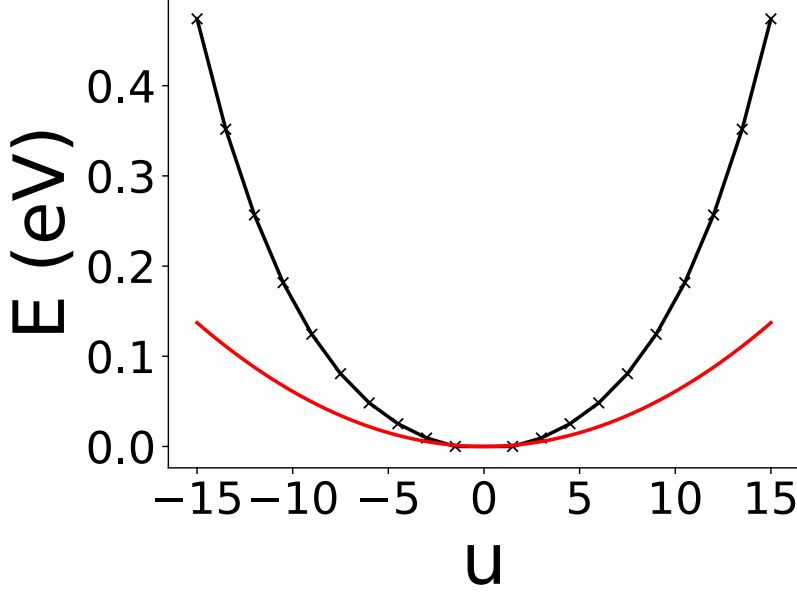


FIG. S3. Comparison between the harmonic (red) and anharmonic (black) potential energy surfaces of the acoustic mode with frequency $\omega = 40 \text{ cm}^{-1}$ at $\mathbf{q} = X$. The phonon displacement u is given in units of the zero-point width $\frac{1}{\sqrt{2\omega}}$.

S4. ANHARMONIC POTENTIAL ENERGY SURFACES

Fig. S3 visualizes the potential energy surface of the anharmonic acoustic mode of pentacene discussed in the main manuscript, at $\mathbf{q} = X$, where it has a frequency of $\omega = 40 \text{ cm}^{-1}$. In red we show the harmonic potential energy surface as predicted by the relationship $E = \frac{1}{2}\omega^2 u^2$, while the black crosses indicate the total energy of the system (with respect to that of the optimized geometry) upon explicitly displacing along this phonon and performing DFT calculations at different displacements u . While for small values of u the two results coincide, they quickly start to diverge, and anharmonicity provides an energetic barrier which prevents the over-displacement of pentacene along this mode, as permitted within the harmonic approximation.

S5. HIGHLY DELOCALIZED EXCITONS WITHIN THE HARMONIC APPROXIMATION

As discussed in the main manuscript, the thermal excitation of phonons within the harmonic approximation leads to configurations with highly delocalized excitons. The most prominent examples appear when the anharmonic acoustic phonon of pentacene, corresponding to a sliding of adjacent molecules along the z -axis, is displaced significantly. Let us consider the case of thermal excitation at 300 K for a $2 \times 1 \times 1$ supercell, which describes this phonon at $\mathbf{q} = X$. In this case, several high-probability hole positions used to sample the electron-hole correlation function of Eq. 5 lead to very large radii in the range of 25–30 Å, for several nuclear geometries. It is worth noting that for some nuclear configurations, it is the hole position with the highest probability entering Eq. 5 which already leads to large exciton radii. As an example, we plot in Fig. S4 the delocalized exciton that arises for a configuration used in the sampling of exciton properties. Here the hole is placed in the most likely position out of the 176 ones used for the sampling of the electron-hole correlation function of the specific nuclear configuration, resulting in an exciton radius of 31 Å. Other examples include two sampled nuclear configurations where the highest probability hole positions lead to excitons with radii of 23 Å and 25 Å. It is also emphasized that for *every* nuclear configuration resulting from thermal phonon excitation at 300 K within the harmonic approximation we find highly probable hole positions that lead to similarly highly delocalized excitons, although in the above three examples these are not only high-probability holes, but the ones with the highest probability.

S6. ESTIMATION OF THE MINIMUM OF THE SINGLET EXCITON POTENTIAL ENERGY SURFACE

We would like to estimate the position of the minimum of the singlet exciton potential energy surface along the acoustic phonon of pentacene, which is responsible for exciton delocalization at large displacements u . To do so, we have to assume the ground and excited state potential energy surfaces to be harmonic. The ground state energy along this phonon will be

$$E_{GS}(u) = \frac{1}{2}\omega_{GS}^2 u^2, \quad (8)$$

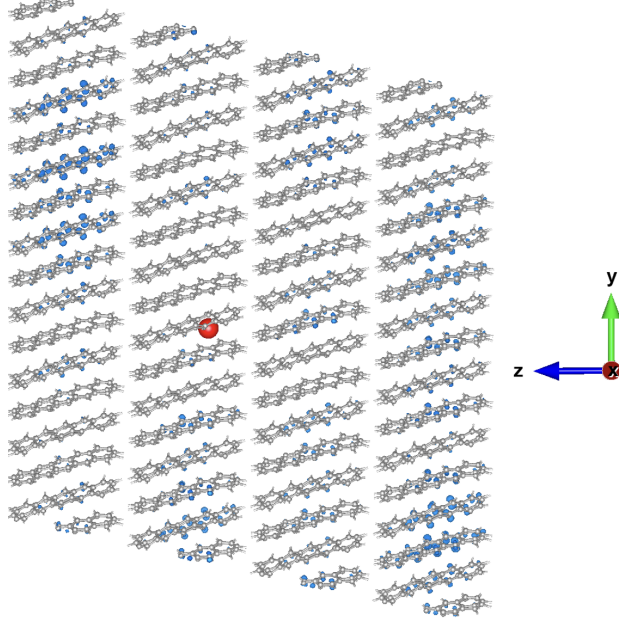


FIG. S4. Isosurface of the electron distribution (blue) for a highly delocalized pentacene singlet exciton, for a hole placed at the position in red. This exciton with a radius of 31 \AA appears within the harmonic approximation for a $2 \times 1 \times 1$, as a result of thermal phonon excitation at 300 K.

where ω_{GS} the phonon frequency in the ground state. Reexpressing the phonon displacement u in units of the zero-point width $1/\sqrt{2\omega}$ of the harmonic distribution, this may be rewritten as

$$E_{GS}(u) = \frac{1}{4}\omega_{GS}u^2. \quad (9)$$

The excited state surface within these units is written as

$$E_{ES}(u) = \frac{1}{4}\omega_{ES}(u - u_{ES})^2 + \Delta, \quad (10)$$

where we have the following unknown quantities: u_{ES} , which is the position at which the excited state obtains its minimum energy, Δ , which is the total energy of the system when in the excited state and at that geometry and ω_{ES} , which is the excited state mode frequency.

We would now like to estimate u_{ES} , for this purpose we perform DFT and *GW*-BSE calculations at $u = 5, 15$ for this phonon mode. At each of these atomic configurations, we obtain the excited state surface energy as the vertical excitation energy (from *GW*-BSE) plus the ground state energy (from DFT), in order to obtain the total energy of the system in the excited state. Solving the resulting system and after a few algebraic manipulations

we find $u_{ES} \approx 1$. While this is a rough estimate, it is clear that the potential energy surface minimum is far from the very large values of u which are required in order to find the highly delocalized excitons that appear for values of u that are equal to 30 or greater (see main manuscript Fig. 3b).

S7. TABLES OF AVERAGES AND STANDARD DEVIATIONS OF EXCITON ENERGIES AND RADII

| $r_{\text{exc}}(T)$ (Å) | singlet | triplet |
|-------------------------|-----------------|-----------------|
| 0 K | 4.85 ± 0.30 | 1.23 ± 0.13 |
| 100 K | 5.04 ± 0.17 | 1.23 ± 0.10 |
| 200 K | 4.98 ± 0.21 | 1.32 ± 0.07 |
| 300 K | 6.96 ± 1.25 | 1.26 ± 0.13 |

TABLE S4. Vibrational averages of exciton radii within the harmonic approximation - $2 \times 1 \times 1$ supercell.

| $r_{\text{exc}}(T)$ (Å) | singlet | triplet |
|-------------------------|-----------------|-----------------|
| 100 K | 5.90 ± 0.65 | 1.48 ± 0.15 |
| 300 K | 5.25 ± 0.35 | 1.57 ± 0.08 |

TABLE S5. Vibrational averages of exciton radii within the anharmonic distribution - $2 \times 1 \times 1$ supercell.

| $E(S_1)(T)$ (eV) | $-X$ | $-X/2$ | Γ | $X/2$ | X |
|------------------|-------------------|-------------------|-------------------|-------------------|-------------------|
| 0 K | 1.771 ± 0.047 | 1.735 ± 0.056 | 1.688 ± 0.064 | 1.737 ± 0.056 | 1.771 ± 0.047 |
| 300 K | 1.730 ± 0.030 | 1.704 ± 0.043 | 1.663 ± 0.053 | 1.706 ± 0.045 | 1.733 ± 0.033 |

TABLE S6. Singlet exciton energies at various points in reciprocal space, including the effect of Γ phonons at 0 K and 300 K within the harmonic approximation.

| $E(T_1)(T)$ (eV) | $-X$ | $-X/2$ | Γ | $X/2$ | X |
|------------------|-------------------|-------------------|-------------------|-------------------|-------------------|
| 0 K | 0.918 ± 0.030 | 0.909 ± 0.027 | 0.898 ± 0.027 | 0.910 ± 0.028 | 0.918 ± 0.030 |
| 300 K | 0.918 ± 0.051 | 0.910 ± 0.048 | 0.899 ± 0.045 | 0.910 ± 0.048 | 0.918 ± 0.052 |

TABLE S7. Triplet exciton energies at various points in reciprocal space, including the effect of Γ phonons at 0 K and 300 K within the harmonic approximation.

| $E(S_1)(T)$ (eV) | Γ | X |
|------------------|-------------------|-------------------|
| 0 K | 1.593 ± 0.064 | 1.654 ± 0.041 |
| 300 K | 1.636 ± 0.064 | 1.712 ± 0.061 |

TABLE S8. Singlet exciton energies at various points in reciprocal space, including the effects of Γ, X phonons at 0 K and 300 K within the harmonic approximation.

| $E(S_1)(T)$ (eV) | Γ | $X/2$ | X |
|------------------|-------------------|-------------------|-------------------|
| 100 K | 1.713 ± 0.037 | 1.739 ± 0.038 | 1.780 ± 0.043 |
| 300 K | 1.695 ± 0.041 | 1.719 ± 0.039 | 1.754 ± 0.038 |

TABLE S9. Singlet exciton energies at various points in reciprocal space, including anharmonic effects and Γ phonons at 100 K and 300 K.

| $E(T_1)(T)$ (eV) | Γ | $X/2$ | X |
|------------------|-------------------|-------------------|-------------------|
| 100 K | 0.885 ± 0.078 | 0.896 ± 0.081 | 0.904 ± 0.083 |
| 300 K | 0.872 ± 0.063 | 0.878 ± 0.068 | 0.891 ± 0.068 |

TABLE S10. Triplet exciton energies at various points in reciprocal space, including anharmonic effects and Γ phonons at 100 K and 300 K.

| $E(S_1)(T)$ (eV) | Γ | $X/2$ | X |
|------------------|-------------------|-------------------|-------------------|
| 100 K | 1.659 ± 0.036 | 1.692 ± 0.033 | 1.718 ± 0.026 |
| 300 K | 1.656 ± 0.046 | 1.675 ± 0.044 | 1.698 ± 0.040 |

TABLE S11. Singlet exciton energies at various points in reciprocal space, including anharmonic effects and Γ, X phonons at 100 K and 300 K.

| $E(T_1)(T)$ (eV) | Γ | $X/2$ | X |
|------------------|-------------------|-------------------|-------------------|
| 100 K | 0.859 ± 0.048 | 0.870 ± 0.037 | 0.877 ± 0.030 |
| 300 K | 0.859 ± 0.037 | 0.865 ± 0.044 | 0.878 ± 0.070 |

TABLE S12. Triplet exciton energies at various points in reciprocal space, including anharmonic effects and Γ, X phonons at 100 K and 300 K.

-
- [1] P. Giannozzi, S. Baroni, N. Bonini, M. Calandra, R. Car, C. Cavazzoni, D. Ceresoli, G. L. Chiarotti, M. Cococcioni, I. Dabo, A. Dal Corso, S. Fabris, G. Fratesi, S. de Gironcoli, R. Gebauer, U. Gerstmann, C. Gougoussis, A. Kokalj, M. Lazzeri, L. Martin-Samos, N. Marzari, F. Mauri, R. Mazzarello, S. Paolini, A. Pasquarello, L. Paulatto, C. Sbraccia, S. Scandolo, G. Sclauzero, A. P. Seitsonen, A. Smogunov, P. Umari, and R. M. Wentzcovitch, QUANTUM ESPRESSO: a modular and open-source software project for quantum simulations of materials, *Journal of Physics: Condensed Matter* **21**, 395502 (2009).
 - [2] J. P. Perdew, K. Burke, and M. Ernzerhof, Generalized Gradient Approximation Made Simple, *Physical Review Letters* **77**, 3865 (1996).
 - [3] S. Haas, B. Batlogg, C. Besnard, M. Schiltz, C. Kloc, and T. Siegrist, Large uniaxial negative thermal expansion in pentacene due to steric hindrance, *Phys. Rev. B* **76**, 1 (2007).
 - [4] A. Tkatchenko and M. Scheffler, Accurate molecular van der Waals interactions from ground-state electron density and free-atom reference data, *Physical Review Letters* **102**, 6 (2009).
 - [5] H. J. Monkhorst and J. D. Pack, Special points for Brillouin-zone integrations, *Phys. Rev. B* **13**, 5188 (1976).
 - [6] J. Deslippe, G. Samsonidze, D. A. Strubbe, M. Jain, M. L. Cohen, and S. G. Louie, BerkeleyGW: A massively parallel computer package for the calculation of the quasiparticle and optical properties of materials and nanostructures, *Computer Physics Communications* **183**, 1269 (2012), [1111.4429](#).
 - [7] S. Refaely-Abramson, F. H. Da Jornada, S. G. Louie, and J. B. Neaton, Origins of Singlet Fission in Solid Pentacene from an ab initio Green's Function Approach, *Physical Review Letters* **119**, 1 (2017), [1706.01564](#).
 - [8] A. M. Alvertis, R. Pandya, L. A. Muscarella, N. Sawhney, M. Nguyen, B. Ehrler, A. Rao, R. H. Friend, A. W. Chin, and B. Monserrat, Impact of exciton delocalization on exciton-vibration interactions in organic semiconductors, *Phys. Rev. B* **102**, 081122 (2020).
 - [9] B. Monserrat, Vibrational averages along thermal lines, *Phys. Rev. B* **93**, 1 (2016), [1512.06377](#).
 - [10] A. M. Alvertis and E. A. Engel, Importance of vibrational anharmonicity for electron-phonon coupling in molecular crystals, *Phys. Rev. B* **105**, 1 (2022).

- [11] Y. Eldar, M. Lindenbaum, M. Porat, and Y. Y. Zeevi, The Farthest Point Strategy for Progressive Image Sampling, *IEEE Transactions on Image Processing* **6**, 1305 (1997).
- [12] R. J. G. B. Campello, D. Moulavi, A. Zimek, and J. Sander, Hierarchical density estimates for data clustering, visualization, and outlier detection, *ACM Trans. Knowl. Discov. Data* **10**, 5 (2015).
- [13] A. P. Bartók, R. Kondor, and G. Csányi, On representing chemical environments, *Phys. Rev. B* **87**, 184115 (2013).
- [14] M. J. Willatt, F. Musil, and M. Ceriotti, Feature optimization for atomistic machine learning yields a data-driven construction of the periodic table of the elements, *Phys Chem Chem Phys* **20**, 29661 (2018).
- [15] A. Singraber, **N2P2**, <https://github.com/CompPhysVienna/n2p2>.
- [16] V. Kapil, M. Rossi, O. Marsalek, R. Petraglia, Y. Litman, T. Spura, B. Cheng, A. Cuzzocrea, R. H. Meißner, D. M. Wilkins, B. A. Helfrecht, P. Juda, S. P. Bienvenue, W. Fang, J. Kessler, I. Poltavsky, S. Vandenbrande, J. Wieme, and M. Ceriotti, i-PI 2.0: A universal force engine for advanced molecular simulations, *Computer Physics Communications* **236**, 214 (2018).
- [17] S. Plimpton, Fast parallel algorithms for short-range molecular dynamics, *J. Comput. Phys.* **117**, 1 (1995).
- [18] M. Ceriotti, M. Parrinello, T. E. Markland, and D. E. Manolopoulos, Efficient stochastic thermostating of path integral molecular dynamics, *J. Chem. Phys.* **133**, 124104 (2010).
- [19] V. Kapil and E. A. Engel, A complete description of thermodynamic stabilities of molecular crystals, *Proc. Natl. Acad. Sci. U.S.A.* **119**, e2111769119 (2022).
- [20] S. Sharifzadeh, P. Darancet, L. Kronik, and J. B. Neaton, Low-Energy Charge-Transfer Excitons in Organic Solids from First-Principles: The Case of Pentacene, *The Journal of Physical Chemistry Letters* **4**, 2197 (2013).
- [21] T. Rangel, K. Berland, S. Sharifzadeh, F. Brown-Altvater, K. Lee, P. Hyldgaard, L. Kronik, and J. B. Neaton, Structural and excited-state properties of oligoacene crystals from first principles, *Phys. Rev. B* **93**, 1 (2016).